

# Numerical study of optimal control domain decomposition for nonlinear boundary heat in the human eye

Salem Ahmedou Bamba\* , Abdellatif Ellabib  
and Abdessamad El Madkouri

*Université Cadi Ayyad, Faculté des Sciences et Techniques, Marrakech,  
Maroc*

*Email(s): salemmohamed39@gmail.com, a.ellabib@uca.ac.ma,  
abdessamad.elmadkouri@edu.uca.ma*

---

**Abstract.** The present work sheds new light on the computation of the heat distribution on the boundary of the human eye. Due to different values of the thermal conductivity on each region of the human eye, the domain decomposition technique is introduced and an optimization formulation is analysed and studied to derive a proposed algorithm. All obtained partial differential equations are approached by discontinuous dual reciprocity boundary element method. The validity of the proposed approaches is confirmed by comparing to results reported with previous experimental and numerical studies.

*Keywords:* Heat distribution, human eye, optimal control, Dirichlet-Neumann, boundary element method.

*AMS Subject Classification 2010:* 65N38, 92C50.

---

## 1 Introduction

Eye disease is the most common cause of blindness, especially in the developing world where early diagnosis are unavailable for treatable diseases. According to the World Health Organization, about 39 million people around

---

\*Corresponding author.

Received: 10 December 2019 / Revised: 6 February 2020 / Accepted: 8 April 2020.  
DOI: 10.22124/jmm.2020.15163.1363

the world are blind and a further 246 million are unable to see properly. More than two millennia ago, Hippocrates found that the disease is expected to be present in parts of the human body where we have an increase or decrease in the temperature. Despite being very old, this concept is still being used by physicians to determine the state of the health of a patient.

For over a century, researchers have been interested in the human eye temperature. In 1875, Dohnberg (cited in [10]) used a mercury thermometer and took a series of measurements of the ocular surface temperature. In normal conditions, he reported a variation between  $35.8^{\circ}\text{C}$  and  $37^{\circ}\text{C}$ . Mapstone [13] Used a bolometer in 1968 to measure the temperature of the ocular surface, he recorded a mean temperature of  $34.8^{\circ}\text{C}$ . In the 1989, Efron et al. [5] used infra-red techniques and reported a mean temperature of  $34.3^{\circ}\text{C}$ , while more recently in 2005, Purslow et al. [19] obtained a mean temperature of  $35 \pm 1.1^{\circ}\text{C}$ . These experimental techniques induce measurement errors and present only the measurements of the ocular surface temperature without much information on the temperature in the interior parts of the human eye. In the 1980s, the development of computing technologies, especially the use of numerical and mathematical investigations, has made it possible to obtain the temperature all over the eyeball without using any experimental devices. In the last decades, computational methods are considered by many researchers as an alternative to experimental techniques. In 1982, Lagendijk [12] used finite difference method (FDM) to obtain the temperature of a rabbit's eye and obtained a mean ocular surface temperature of  $34.5^{\circ}\text{C}$ . In 1988, Scott [21] using a finite element method (FEM) recorded a temperature of  $33.25^{\circ}\text{C}$  at the surface of the cornea. In 2006, Ng et al. [15] obtained results of the heat distribution all over the human eye using finite element method (FEM). They recorded a mean ocular surface temperature of  $33.65^{\circ}\text{C}$ . In 2007, Ooi et al. [16] investigated the bioheat transfer in the eye using boundary element method (BEM) approach and reported a mean ocular surface temperature of  $33.68^{\circ}\text{C}$ . In another work in 2008, Ooi et al. [17] investigated the aqueous humor hydrodynamics effects in human eye heat transfer. More recently Wang et al. [22] used finite element approach with Greens function as internal trial function for simulating bioheat transfer in the human eye. A study of heat transfer in human eye undergoing laser surgery was done in [14], where the authors used transient simulations to predict heat behaviour.

In this work a combination between discontinuous dual reciprocity boundary element method and non-overlapping domain decomposition method [2] is used to obtain an approximation of heat distribution in the human eye. Two types of non-overlapping domain decomposition method are adopted

in this study, namely the Dirichlet-Neumann method and a combination between optimization techniques and non-overlapping domain decomposition. This paper is divided into five sections, in the first section the governing equation of heat distribution in human eye is presented with adequate boundary conditions, the second section is dedicated to the description of the proposed approach, in the fourth section some numerical applications are presented and in the final section a conclusion is drawn.

## 2 Mathematical formulation

### 2.1 The human eye model

A two-dimensional model of the human eye following the dimensions in [15], is developed in this section. The human eye model is obtained using anatomical measurements reported in the literature [3,7]. In this model, the eye is partitioned into four parts the aqueous humor, the lens, the vitreous humor and the sclera as in Figure 1 with different thermal properties. The retina and the choroid are very thin and are considered as part of the sclera. The iris and the sclera has similar thermal properties and are modeled together. Since the cornea and the aqueous humor have similar thermal properties [4], the cornea is assumed to be part of the aqueous humor. The thermal properties of the human eye are given in Table 1. In this work, the human eye is decomposed into two domains, namely the aqueous humor and the lens noted  $\Omega_1$  and the vitreous humor and the sclera denoted as  $\Omega_2$ .

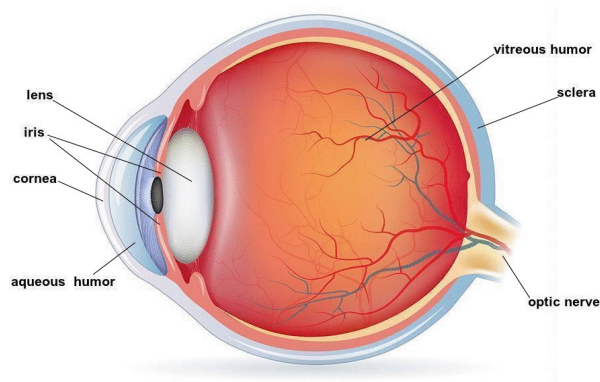


Figure 1: 2D illustration of the human eye.

## 2.2 Governing equation

The equation governing heat distribution in the human eye is Pennes bio-heat equation is given in [18] and is written as in

$$\rho c_b \frac{\partial T}{\partial t} = \nabla(k\nabla T) + \omega_b \rho_b c_b (T_b - T) + Q + Q_m, \quad (1)$$

where  $T$  is the temperature ( $K$ ),  $\rho$  is the density ( $kg\ m^{-3}$ ),  $c_b$  the specific heat ( $J\ kg^{-1}\ K^{-1}$ ),  $k$  the thermal conductivity of local tissue ( $W\ m^{-1}\ K^{-1}$ ),  $\omega_b$  is the volumetric flow rate of blood in the eye ( $m^3/s$ ),  $t$  is time ( $s$ ),  $Q_m$  is heat generated through metabolism ( $W\ m^{-3}$ ) and  $Q$  is heat generated from external sources such as radiation. Subscript  $b$  refers to blood.

Heat generated by metabolism or by external source is neglected because the human eye is composed mainly of water and we assume that there is no radiations affecting the heat in human eye. For a steady state case, Eq. (1) is written

$$\nabla(k\nabla T) + \omega_b \rho_b c_b (T_b - T) = 0. \quad (2)$$

The thermal conductivity of each sub-domain can be found in Table 1.

Moreover,  $T_b$  is the blood temperature  $37^\circ C$ ,  $c_b$  is the specific heat of blood  $3594\ J/kg^\circ K$  and  $\rho_b$  is the density of blood which are equal to and  $1060\ kg/m^3$  [15].

Table 1: Properties of different tissues of the human eye [9].

Tissue	Thermal conductivity ( $Wm^{-1}K^{-1}$ )	Blood perfusion rate ( $m^3/s$ )
<i>Cornea</i>	0.58	0
<i>Aqueous humor</i>	0.58	0
<i>Lens</i>	0.40	0
<i>Iris</i>	1.0042	0
<i>Vitreous humor</i>	0.603	0
<i>Choroid</i>	0.53	0.021
<i>Retina</i>	0.565	0.035
<i>Sclera</i>	1.0042	0

## 2.3 Boundary conditions

Boundary conditions are defined on the surfaces of the cornea and the sclera as follow:

- On the surface of the sclera  $\Gamma_s$ , the blood flow is acting as a heating source

$$-k \frac{\partial T}{\partial n} = h_{bl}(T - T_{bl}). \quad (3)$$

In the above equation,  $n$  is the normal direction to the surface boundary.  $h_{bl}$  ( $65 \text{ Wm}^{-2}\text{K}^{-1}$ ) is the convection coefficient between blood and eye and  $T_{bl}$  is blood temperature ( $37^\circ\text{C}$ ) [15].

- On the surface of the cornea  $\Gamma_c$ , there are three forms of heat loss through convection, radiation and tears evaporation.

$$-k \frac{\partial T}{\partial n} = h_{amb}(T - T_{amb}) + \sigma\varepsilon(T^4 - T_{amb}^4) + E. \quad (4)$$

In this equation,  $T_{amb}$  is the ambient temperature ( $25^\circ\text{C}$ ),  $h_{amb}$  is the convection coefficient ( $10 \text{ Wm}^{-2}\text{K}^{-1}$ ) and  $E$  is the tear evaporation rate of the eye ( $40 \text{ Wm}^{-2}$ ).  $\sigma$  is the Stefan Boltzmann constant ( $5.67 \times 10^{-8} \text{ Wm}^{-2}\text{K}^{-4}$ ) and  $\varepsilon$  is emissivity 0.975 [15].

Then, the non-linear boundary problem for heat distribution in the human eye, in stationary state, can be written as follows:

$$\begin{cases} -\nabla(k\nabla T) + \omega_b\rho_b c_b T = \omega_b\rho_b c_b T_b & \text{in } \Omega, \\ -k \frac{\partial T}{\partial n} = h_{bl}(T - T_{bl}) & \text{on } \Gamma_s, \\ -k \frac{\partial T}{\partial n} = h_{amb}(T - T_{amb}) + \sigma\varepsilon(T^4 - T_{amb}^4) + E & \text{on } \Gamma_c. \end{cases} \quad (5)$$

We are interested now in approximating problem (5). Due to the different values of thermal conductivity of local tissue, we can decompose the human eye  $\Omega$  into two domains  $\Omega_1$  and  $\Omega_2$ .  $\Omega_1$  is composed of the cornea, the aqueous humor and the lens and  $\Omega_2$  is formed by the sclera, the vitreous humor and the iris.

### 3 Description and analysis of algorithms

In this section, our domain decomposition is illustrated in Figure 2 and we begin by describing the obtained Dirichlet-Neumann method.

#### 3.1 Dirichlet-Neumann domain decomposition method

The first domain decomposition technique is done using Dirichlet-Neumann decomposition method and by decomposing the human eye into two disjoint sub-domains  $\Omega_1$  and  $\Omega_2$  presented in Figure 2.  $I$  is the interface between

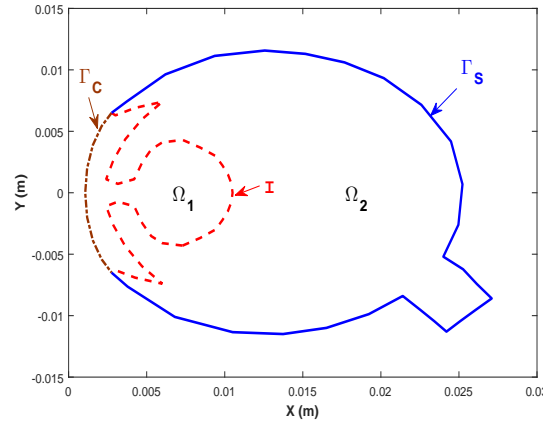


Figure 2: The decomposition of the human eye into two subdomains. The first subdomain is  $\Omega_1$  composed of the cornea and the lens and the second subdomain  $\Omega_2$  is constituted of the iris, the vitreous humor and the sclera.

---

**Algorithm 1** Dirichlet-Neumann domain decomposition algorithm

---

Input:  $Tol$ ,  $\mu_0$ ,  $k = 1$ , and  $error = 1$

While  $error \geq Tol$

- Solve non-linear problem (6) to obtain  $\frac{\partial T_1^k}{\partial n_1}$  on  $I$ :

$$\begin{cases} -\nabla(k_1 \nabla T_1^k) + \omega_b \rho_b c_b T_1^k = \omega_b \rho_b c_b T_b & \text{in } \Omega_1 \\ -k_1 \frac{\partial T_1^k}{\partial n_1} = h_{amb}(T_1^k - T_{amb}) + \sigma \varepsilon ((T_1^k)^4 - T_{amb}^4) + E & \text{on } \Gamma_c \\ T_1^k = \mu_{k-1} & \text{on } I \end{cases} \quad (6)$$

- Solve linear problem (7) to obtain  $T_2^k$  on  $I$ :

$$\begin{cases} -\nabla(k_2 \nabla T_2^k) + \omega_b \rho_b c_b T_2^k = \omega_b \rho_b c_b T_b & \text{in } \Omega_2 \\ -k_2 \frac{\partial T_2^k}{\partial n_2} = h_{bl}(T_2^k - T_{bl}) & \text{on } \Gamma_s \\ -k_2 \frac{\partial T_2^k}{\partial n_2} = k_1 \frac{\partial T_1^k}{\partial n_1} & \text{on } I \end{cases} \quad (7)$$

- Update:

$$\mu_k = \mu_{k-1} + \theta(T_2^k - \mu_{k-1}) \text{ on } I \text{ and } \theta \in ]0, 1[$$

- Compute:

$$error = \|\mu_k - \mu_{k-1}\|, \quad k = k + 1$$

End while

---

sub-domains  $\Omega_1$  and  $\Omega_2$ . The Dirichlet-Neumann algorithm used to solve

problem (5) is given by Algorithm 1.

The non-linearity in (6) is treated using Newton’s method [8]. We are interesting to propose an algorithm based on optimization formulation and it is described and analysed in the following section.

### 3.2 Optimal control formulation

In this section, the human eye is also divided into two disjoint sub-domains  $\Omega_1$  and  $\Omega_2$  illustrated in Figure 2.  $I$  is the interface between sub-domains  $\Omega_1$  and  $\Omega_2$ . For given  $\psi$ , the problem (5) defined over these two sub-domains is then given on  $\Omega_1$  by

$$\begin{cases} -\nabla(k_1\nabla T_1) + \omega_b\rho_b c_b T_1 = \omega_b\rho_b c_b T_b & \text{in } \Omega_1, \\ -k_1 \frac{\partial T_1}{\partial n_1} = h_{amb}(T_1 - T_{amb}) + \sigma\varepsilon((T_1)^4 - T_{amb}^4) + E & \text{on } \Gamma_c, \\ k_1 \frac{\partial T_1}{\partial n_1} = \psi & \text{on } I, \end{cases} \quad (8)$$

and on  $\Omega_2$  by

$$\begin{cases} -\nabla(k_2\nabla T_2) + \omega_b\rho_b c_b T_2 = \omega_b\rho_b c_b T_b & \text{in } \Omega_2, \\ -k_2 \frac{\partial T_2}{\partial n_2} = h_{bl}(T_2 - T_{bl}) & \text{on } \Gamma_s, \\ k_2 \frac{\partial T_2}{\partial n_2} = -\psi & \text{on } I. \end{cases} \quad (9)$$

In this part, the interest is to combine an optimal control formulation and non-overlapping domain decomposition to solve problem (5). This combination is given as a constrained minimization problem where the cost functional is the  $L^2(I)$ -norm of the difference between  $T_1$  and  $T_2$  across the interface  $I$  where  $T_1$  and  $T_2$  are the solutions of the state equations (8) and (9), respectively. Our goal is to determine a function such that  $T_1$  is as close as possible to  $T_2$  along the interface  $I$ . Mathematically, the optimal control formulation is defined as follows:

$$\begin{cases} \text{Minimize } J(T_1(\psi), T_2(\psi)) \text{ for all } \psi \in V_0 \\ \text{where } J(T_1(\psi), T_2(\psi)) = \frac{1}{2} \int_I (T_1 - T_2)^2 ds \\ T_1(\psi), T_2(\psi) \text{ solutions of (8) and (9), respectively.} \end{cases} \quad (10)$$

$V_0$  is the convex set given by:

$$V_0 = \{\psi \in L^2(I) \mid \|\psi\|_{L^2(I)} \leq C\},$$

where  $C \geq 0$ .

**Remark 1.** *The equivalence between problem (5) and (10) can be verified easily.*

For  $\psi \in V_0$ , the weak formulation of problem (8) is given by

$$\begin{cases} \mathbf{Find} & T_1(\psi) \in H^1(\Omega_1) \\ \forall v_1 \in H^1(\Omega_1) & a_1(T_1(\psi), v_1) + h(T_1(\psi), v_1) = L_1(v_1) \end{cases} \quad (11)$$

where

$$\begin{aligned} a_1(T_1(\psi), v_1) &= \int_{\Omega_1} (k_1 \nabla T_1(\psi) \nabla v_1 + \omega_b \rho_b c_b T_1(\psi) v_1) d\Omega_1 \\ &\quad + \int_{\Gamma_c} h_{amb} T_1(\psi) v_1 ds, \\ h(T_1(\psi), v_1) &= \int_{\Gamma_c} \sigma \varepsilon T_1^4(\psi) v_1 ds, \end{aligned}$$

and

$$\begin{aligned} L_1(v_1) &= \int_{\Omega_1} \omega_b \rho_b c_b T_b v_1 d\Omega_1 + \int_I \psi v_1 ds \\ &\quad + \int_{\Gamma_c} (h_{amb} T_{amb} + h_{amb} T_{amb}^4 - E) v_1 ds. \end{aligned}$$

For  $\psi \in V_0$ , the weak formulation of problem (9) is given by

$$\begin{cases} \mathbf{Find} & T_2(\psi) \in H^1(\Omega_2) \\ \forall v_2 \in H^1(\Omega_2) & a_2(T_2(\psi), v_2) = L_2(v_2) \end{cases} \quad (12)$$

where

$$\begin{aligned} a_2(T_2(\psi), v_2) &= \int_{\Omega_2} (k_2 \nabla T_2(\psi) \nabla v_2 + \omega_b \rho_b c_b T_2(\psi) v_2) d\Omega_2 \\ &\quad + \int_{\Gamma_s} h_{bl} T_2(\psi) v_2 ds, \end{aligned}$$

and

$$L_2(v_2) = \int_{\Omega_2} \omega_b \rho_b c_b T_b v_2 d\Omega_2 - \int_I \psi v_2 ds + \int_{\Gamma_s} h_{bl} T_{bl} v_1 ds.$$

The space of admissible solutions is defined by:

$$U_{ad} = \{(T_1(\psi), T_2(\psi)) \text{ solutions of (11) and (12) and } \psi \in V_0\}.$$

$U_{ad}$  is equipped with the topology defined by the following convergence:

Let  $(T_1^n, T_2^n)_n$  be a sequence of  $U_{ad}$  and  $(T_1, T_2) \in U_{ad}$  then:

$$(T_1^n, T_2^n)_n \rightarrow (T_1, T_2) \iff \begin{cases} T_1^n \rightharpoonup T_1 \text{ in } H^1(\Omega_1), \\ T_2^n \rightharpoonup T_2 \text{ in } H^1(\Omega_2). \end{cases} \quad (13)$$

The optimal control problem (10) can be rewritten as

$$\text{Minimize } J(T_1(\psi), T_2(\psi)) \text{ for all } (T_1(\psi), T_2(\psi)) \in U_{ad}. \quad (14)$$

**Theorem 1.** *The problem (14) is well posed and admits a solution in  $U_{ad}$ .*

*Proof.* For all  $\psi \in V_0$

$$\text{(P)} \quad \forall v_1 \in H^1(\Omega_1) \quad a_1(T_1(\psi), v_1) + h(T_1(\psi), v_1) = L_1(v_1).$$

By taking  $B(T_1(\psi)) = T_1^5(\psi)/5$ , the problem (P) is equivalent to the following optimization problem:

$$\min_{T_1(\psi) \in H^1(\Omega_1)} G(T_1(\psi)),$$

where

$$G(T_1(\psi)) = \frac{1}{2}a_1(T_1(\psi), T_1(\psi)) + \int_{\Gamma_c} \sigma \varepsilon B(T_1(\psi)) ds - L_1(T_1(\psi)).$$

We can prove easily that the application  $G$  is strictly convex, coercive, semi-continuous inferiorly. Hence the existence and uniqueness of the solution of (P). The result of the existence and uniqueness of the solution of the other weak formulation in (12) is ensured by the Lax-Milgram theorem, this confirms that the problem (14) is well posed.

To proof of the existence of a solution of (11) and (12) is now reduced to show that the space  $U_{ad}$  is compact and that  $J$  is lower semi-continuous on  $U_{ad}$ . To show that  $U_{ad}$  is compact for the topology defined by (13), let  $(T_1^n, T_2^n)_n$  be a sequence of  $U_{ad}$ .  $(T_1^n, T_2^n)_n = (T_1(\psi_n), T_2(\psi_n))$  solutions of (10) for  $\psi_n \in V_0$ . Since  $\forall n \|\psi_n\| \leq C$ , the a subsequence denoted again  $(\psi_n)_n$  can be extracted, such that  $\psi_n$  converges weakly in  $L^2(I)$  to  $\psi^* \in V_0$ . In the other hand, we can see that the sequences  $(T_1^n)_n$  and  $(T_2^n)_n$  are bounded in  $H^1(\Omega_1)$  and  $H^1(\Omega_2)$ , respectively. Thus the sequence  $(T_1^n, T_2^n)_n$  converges weakly to  $(T_1^*, T_2^*)$ . The remaining is to prove that  $(T_1^*, T_2^*) = (T_1(\psi^*), T_2(\psi^*))$ . This is achieved by taking the limit in the following:

$$a_1(T_1(\psi_n), v_1) + h(T_1(\psi_n), v_1) = L_1(v_1) \text{ and } a_2(T_2(\psi_n), v_2) = L_2(v_2).$$

This completes the proof of the compactness of  $U_{ad}$  for the topology defined in (13).

To prove the continuity of  $J$  in  $U_{ad}$ , let  $(T_1^n, T_2^n)_n$  be a sequence in  $U_{ad}$  convergent to  $(T_1, T_2) \in U_{ad}$ . We have

$$\begin{aligned} J(T_1^n, T_2^n) - J(T_1, T_2) &= \frac{1}{2} \int_I ((T_1^n - T_2^n)^2 - (T_1 - T_2)^2) ds \\ &\leq \frac{1}{2} A_n^{\frac{1}{2}} B_n^{\frac{1}{2}}, \end{aligned}$$

where

$$\begin{aligned} A_n &= \int_I (T_1^n - T_1 + T_2 - T_2^n)^2 ds, \\ B_n &= \int_I (T_1^n - T_2^n + T_1 - T_2)^2 ds. \end{aligned}$$

By using, the uniform boundedness of  $(T_1^n)_n$  and  $(T_2^n)_n$  in  $H^1(\Omega_1)$  and  $H^1(\Omega_2)$ , respectively, and the compactness of the trace operator from  $H^1(\Omega_1)$  to  $L^2(I)$  and from  $H^1(\Omega_2)$  to  $L^2(I)$ , we have  $\lim_{n \rightarrow \infty} J(T_1^n, T_2^n) - J(T_1, T_2) = 0$ , which completes the proof.  $\square$

The Lagrange multiplier rule is used to derive the optimality system of equations from which the solutions of the problem (14) can be determined. Let  $\lambda_1 \in H^1(\Omega_1)$ ,  $\lambda_2 \in H^1(\Omega_2)$  and  $\psi \in L^2(I)$ . The Lagrangian is defined by:

$$\begin{aligned} \mathbb{L}(T_1, T_2, \psi, \lambda_1, \lambda_2) &= J(T_1(\psi), T_2(\psi)) - \int_{\Omega_1} k_1 \nabla T_1(\psi) \nabla \lambda_1 d\Omega_1 \\ &+ \int_{\Omega_1} \omega_b \rho_b c_b T_1(\psi) \lambda_1 d\Omega_1 + \int_{\Gamma_c} h_{amb} T_1(\psi) \lambda_1 ds - \int_{\Gamma_c} \sigma \varepsilon T_1^4(\psi) \lambda_1 ds \\ &+ \int_{\Omega_1} \omega_b \rho_b c_b T_b \lambda_1 d\Omega_1 + \int_I \psi \lambda_1 ds + \int_{\Gamma_c} (h_{amb} T_{amb} + h_{amb} T_{amb}^4 - E) \lambda_1 ds \\ &- \int_{\Omega_2} (k_2 \nabla T_2(\psi) \nabla \lambda_2 + \omega_b \rho_b c_b T_2(\psi) \lambda_2) d\Omega_2 + \int_{\Gamma_s} h_{bl} T_2(\psi) \lambda_2 ds \\ &+ \int_{\Omega_2} \omega_b \rho_b c_b T_b \lambda_2 d\Omega_2 - \int_I \psi \lambda_2 ds + \int_{\Gamma_s} h_{bl} T_{bl} \lambda_1 ds. \end{aligned}$$

By setting to zero the first variations with respect to  $\lambda_1$  and  $\lambda_2$  yields to the constraints (11) and (12). Setting to zero the first variations with respect to  $T_1$  and  $T_2$  yields to the adjoint equations.

$$a_1(v, \lambda_1) + \int_{\Gamma_c} 4v^3 \lambda_1 ds = (T_1 - T_2, v)_I \quad \forall v \in H^1(\Omega_1), \quad (15)$$

and

$$a_2(v, \lambda_2) = -(T_1 - T_2, v)_I \quad \forall v \in H^1(\Omega_2), \quad (16)$$

respectively. Then the adjoint equations are given by

$$\begin{cases} -\nabla(k_1\nabla\lambda_1) + \omega_b\rho_b c_b\lambda_1 = 0 & \text{in } \Omega_1, \\ -k_1\frac{\partial\lambda_1}{\partial n_1} = h_{amb}\lambda_1 + 4\sigma\varepsilon(T_1)^3\lambda_1 & \text{on } \Gamma_c, \\ k_1\frac{\partial\lambda_1}{\partial n_1} = T_1 - T_2 & \text{on } I, \end{cases} \quad (17)$$

and

$$\begin{cases} -\nabla(k_2\nabla\lambda_2) + \omega_b\rho_b c_b\lambda_2 = 0 & \text{in } \Omega_2, \\ -k_2\frac{\partial\lambda_2}{\partial n_2} = h_{amb}\lambda_2 & \text{on } \Gamma_s, \\ k_2\frac{\partial\lambda_2}{\partial n_2} = -(T_1 - T_2) & \text{on } I. \end{cases} \quad (18)$$

Minimizing  $\mathbb{J}(\psi) := J(T_1(\psi), T_2(\psi))$  with respect to  $\psi$  is equivalent to the minimization problem (14). The first derivative of  $\mathbb{J}$  is defined as follows

$$\left\langle \frac{d\mathbb{J}}{d\psi}, \tilde{\psi} \right\rangle = \left( T_1(\psi) - T_2(\psi), T_1(\tilde{\psi}) - T_2(\tilde{\psi}) \right) \quad \forall \tilde{\psi} \in L^2(I), \quad (19)$$

where  $T_1(\tilde{\psi}) \in H^1(\Omega_1)$  is solution of

$$a_1(T_1(\tilde{\psi}), v) + \int_{\Gamma_c} 4v^3 T_1(\tilde{\psi}) ds = \left( \tilde{\psi}, v \right)_I \quad \forall v \in H^1(\Omega_1), \quad (20)$$

and  $T_2(\tilde{\psi}) \in H^1(\Omega_2)$  is the solution of

$$a_2(T_2(\tilde{\psi}), v) = - \left( \tilde{\psi}, v \right)_I \quad \forall v \in H^1(\Omega_2). \quad (21)$$

By setting  $v = \lambda_1$  in (20),  $v = \lambda_2$  in (21),  $v = T_1(\tilde{\psi})$  in (15) and  $v = T_2(\tilde{\psi})$  in (16), we get:

$$\frac{d\mathbb{J}}{d\psi} = \lambda_1 - \lambda_2 \quad \text{on } I \quad (22)$$

At this stage, we can present the algorithm 2.

The sensitivity problems (27) and (28) are solved to obtain the dynamic decreasing direction  $\rho^k$ .

All problem presented above requires the solution of boundary, and adequate discretization for numerical realization is boundary element method and the use of dual reciprocity method is a good choice because this method doesn't need a domain discretization only few nodes in internal domain and the discretization of the boundary. We describe in the following section this method.

---

**Algorithm 2** Optimal control domain decomposition algorithm
 

---

Input:  $Tol$ ,  $\psi_0$ ,  $k = 1$ , and  $error = 1$

While  $error \geq Tol$

- Solve non-linear problem (23) to obtain  $T_1^k$  on  $I$ :

$$\begin{cases} -\nabla(k_1 \nabla T_1^k) + \omega_b \rho_b c_b T_1^k = \omega_b \rho_b c_b T_b & \text{in } \Omega_1 \\ -k_1 \frac{\partial T_1^k}{\partial n_1} = h_{amb}(T_1^k - T_{amb}) + \sigma \varepsilon ((T_1^k)^4 - T_{amb}^4) + E & \text{on } \Gamma_c \\ k_1 \frac{\partial T_1^k}{\partial n_1} = \psi_{k-1} & \text{on } I \end{cases} \quad (23)$$

- Solve linear problem (24) to obtain  $T_2^k$  on  $I$ :

$$\begin{cases} -\nabla(k_2 \nabla T_2^k) + \omega_b \rho_b c_b T_2^k = \omega_b \rho_b c_b T_b & \text{in } \Omega_2 \\ -k_2 \frac{\partial T_2^k}{\partial n_2} = h_{bl}(T_2^k - T_{bl}) & \text{on } \Gamma_s \\ k_2 \frac{\partial T_2^k}{\partial n_2} = -\psi_{k-1} & \text{on } I \end{cases} \quad (24)$$

- Solve the adjoint problem (25) to obtain  $\lambda_1^k$  on  $I$ :

$$\begin{cases} -\nabla(k_1 \nabla \lambda_1^k) + \omega_b \rho_b c_b \lambda_1^k = 0 & \text{in } \Omega_1 \\ -k_1 \frac{\partial \lambda_1^k}{\partial n_1} = h_{amb} \lambda_1^k + 4\sigma \varepsilon (T_1^k)^3 \lambda_1^k & \text{on } \Gamma_c \\ k_1 \frac{\partial \lambda_1^k}{\partial n_1} = T_1^k - T_2^k & \text{on } I \end{cases} \quad (25)$$

- Solve the adjoint problem (26) to obtain  $\lambda_2^k$  on  $I$ :

$$\begin{cases} -\nabla(k_2 \nabla \lambda_2^k) + \omega_b \rho_b c_b \lambda_2^k = 0 & \text{in } \Omega_2 \\ -k_2 \frac{\partial \lambda_2^k}{\partial n_2} = h_{bl} \lambda_2^k & \text{on } \Gamma_s \\ k_2 \frac{\partial \lambda_2^k}{\partial n_2} = -(T_1^k - T_2^k) & \text{on } I \end{cases} \quad (26)$$

- Update:  $\nabla J(\psi^k) = \lambda_1^k - \lambda_2^k$ ,  $\zeta^k = \frac{\|\nabla J(\psi^k)\|}{\|\nabla J(\psi^{k-1})\|}$  and  $w^k = \nabla J(\psi^k) - \zeta^k d^{k-1}$

- Solve the sensitivity problem (27) to obtain  $S_1^k$  on  $I$ :

$$\begin{cases} -\nabla(k_1 \nabla S_1^k) + \omega_b \rho_b c_b S_1^k = 0 & \text{in } \Omega_1 \\ -k_1 \frac{\partial S_1^k}{\partial n_1} = h_{amb} S_1^k + 4\sigma \varepsilon (T_1^k)^3 S_1^k & \text{on } \Gamma_c \\ k_1 \frac{\partial S_1^k}{\partial n_1} = w^k & \text{on } I \end{cases} \quad (27)$$

- Solve the sensitivity problem (28) to obtain  $S_2^k$  on  $I$ :

$$\begin{cases} -\nabla(k_2 \nabla S_2^k) + \omega_b \rho_b c_b S_2^k = 0 & \text{in } \Omega_2 \\ -k_2 \frac{\partial S_2^k}{\partial n_2} = h_{bl} S_2^k & \text{on } \Gamma_s \\ k_2 \frac{\partial S_2^k}{\partial n_2} = -w^k & \text{on } I \end{cases} \quad (28)$$

- Update:  $\rho^k = \frac{(T_1^k - T_2^k, S_1^k - S_2^k)}{\|S_1^k - S_2^k\|^2}$  and  $\psi^{k+1} = \psi^k - \rho^k d^k$

- Compute:  $error = \|\nabla J(\psi^k)\|$ ,  $k = k + 1$

End while

---

### 4 Discontinuous dual reciprocity boundary element method

In this section, a dual reciprocity boundary element approach is adopted to investigate the numerical solution of the problem (5). To develop an integro-differential equation of the considered problem with respect to regions  $\Omega_i, i = 1, 2$ , (as illustrated in Figure 2) a dual reciprocity boundary element method is adopted, that is :

$$\begin{aligned} \lambda(x, y)T_i(x, y) = & \int_{\Gamma_i} T_i(p, q) \frac{\partial T^*}{\partial n}(p, q; x, y) dS(p, q) \\ & - \int_{\Gamma_i} T^*(p, q; x, y) \frac{\partial T_i}{\partial n}(p, q) dS(p, q) \\ & + \int_{\Omega_i} T^*(p, q; x, y) \left[ \frac{w_b \rho_b c_b}{k_i} (T_b - T_i) \right] d\Omega_i(p, q), \end{aligned} \tag{29}$$

for  $(p, q) \in \Omega_i \cup \Gamma_i$  and  $i = 1, 2$ , and the jump term is:

$$\lambda(p, q) = \begin{cases} 1, & (p, q) \in \Omega_i, \\ 0.5, & (p, q) \in \Gamma_i, \\ 0, & \text{otherwise.} \end{cases}$$

The fundamental solution  $T^*(p, q; x, y)$  is written:

$$T^*(p, q; x, y) = -\frac{1}{2\pi} \log \left( \sqrt{((x - p)^2 + (y - q)^2)} \right)$$

The next step is devoted to the discretization of the boundaries  $\Gamma_i$  into  $N_i$  elements, where for each element  $\Gamma_i^{(j)}$  two points  $(x_i^{(j)}, y_i^{(j)})$  and  $(x_i^{(N_i+j)}, y_i^{(N_i+j)})$  are chosen accordingly to the following expressions:

$$\begin{aligned} (x_i^{(j)}, y_i^{(j)}) &= (p_i^{(j)}, q_i^{(j)}) + \tau(p_i^{(j+1)} - p_i^{(j)}, q_i^{(j+1)} - q_i^{(j)}), \\ (x_i^{(N_i+j)}, y_i^{(N_i+j)}) &= (p_i^{(j)}, q_i^{(j)}) + (1 - \tau)(p_i^{(j+1)} - p_i^{(j)}, q_i^{(j+1)} - q_i^{(j)}), \end{aligned}$$

where the two points  $(p_i^{(j)}, q_i^{(j)})$  and  $(p_i^{(j+1)}, q_i^{(j+1)})$  denotes the ends points of the element  $\Gamma_i^{(j)}$ , respectively, for  $j = 1, 2, \dots, N_i$ , and  $\tau \in ]0, 0.5[$ .

We perform a linear approximation of the temperature and the heat flux (denoted  $Q_i(p, q)$ ) in the following form:

$$\begin{aligned} T_i(p, q) &\simeq [1 - d_i^{(j)}(p, q)]T_i^{(j)} + d_i^{(j)}(p, q)T_i^{(N_i+j)}, \\ Q_i(p, q) &\simeq [1 - d_i^{(j)}(p, q)]Q_i^{(j)} + d_i^{(j)}(p, q)Q_i^{(N_i+j)}, \end{aligned}$$

where

$$d_i^{(j)}(p, q) = \frac{\sqrt{(p - p_i^{(j)})^2 + (q - q_i^{(j)})^2} - \tau l_i^{(j)}}{(1 - 2\tau)l_i^{(j)}},$$

$T_i^{(j)}$  and  $T_i^{(N_i+j)}$  denote the temperature at the points  $(x_i^{(j)}, y_i^{(j)})$  and  $(x_i^{(N_i+j)}, y_i^{(N_i+j)})$ , respectively, and  $Q_i^{(j)}$  and  $Q_i^{(N_i+j)}$  denote the heat flux at the points  $(x_i^{(j)}, y_i^{(j)})$  and  $(x_i^{(N_i+j)}, y_i^{(N_i+j)})$ , respectively,  $l_i^{(j)}$  is the length of the element  $\Gamma_i^{(j)}$ . The task of taking the domain integral in (29) to the boundary is achieved by using a radial basis function approximation of the integrand, in other words we have:

$$\left[ \frac{w_b \rho_b c_b}{k_i} (T_b - T_i(p, q)) \right] \simeq \sum_{j=1}^{2N_i+L_i} \alpha^{(j)} R^{(j)}(p, q; p^{(j)}, q^{(j)}), \quad (30)$$

where  $L_i$  is the number of internal collocation points in the domain  $D_i$  and the radial basis function  $R^{(j)}(p, q)$  is given by:

$$R^{(j)}(p, q; p^{(j)}, q^{(j)}) = 1 + ((p - p^{(j)})^2 + (q - q^{(j)})^2) + ((p - p^{(j)})^2 + (q - q^{(j)})^2)^{3/2}.$$

The particular solution  $\hat{T}$  and the radial basis function are related through the relation

$$\Delta \hat{T} = R.$$

Hence the system (29) can be written as follows :

$$\begin{aligned} \lambda(x^{(s)}, y^{(s)}) T_i^{(s)} &= \sum_{k=1}^{N_i} H_{1i}^{(k)}(x^{(s)}, y^{(s)}) T_i^{(k)} + H_{2i}^{(k)}(x^{(s)}, y^{(s)}) T_i^{(N_i+k)} \\ &\quad - G_{1i}^{(k)}(x^{(s)}, y^{(s)}) Q_i^{(k)} - G_{2i}^{(k)}(x^{(s)}, y^{(s)}) Q_i^{(N_i+k)} \\ &= \sum_{j=1}^{2N_i+L_i} \sum_{k=1}^{N_i} H_{1i}^{(k)}(x^{(s)}, y^{(s)}) T_i^{(k)} + H_{2i}^{(k)}(x^{(s)}, y^{(s)}) T_i^{(N_i+k)} \\ &\quad - G_{1i}^{(k)}(x^{(s)}, y^{(s)}) Q_i^{(k)} - G_{2i}^{(k)}(x^{(s)}, y^{(s)}) Q_i^{(N_i+k)} \\ &\quad \times \sum_{e=1}^{2N_i+L_i} W_i^{(je)} \left[ \frac{w_b \rho_b c_b}{k_i} (T_b - T_i^{(j)}) \right], \end{aligned}$$

For  $s = 1, 2, \dots, 2N_i + L_i$  and  $i = 1, 2$ , where  $W_i^{(je)}$  are the coefficients of the inverse of the matrix  $R_i$ . The system (31) constitutes  $2N_i$  unknowns (the temperature) and  $L_i$  internal unknown  $T_i^{(s)}$  for  $s = 2N_i + 1, \dots, 2N_i + L_i$ .

The line integrals  $H_{1i}^{(k)}$ ,  $H_{2i}^{(k)}$ ,  $G_{1i}^{(k)}$  and  $G_{2i}^{(k)}$  are defined by

$$\begin{aligned} H_{1i}^{(k)}(x, y) &= \int_{\Gamma^k} (1 - d_i^{(k)}) \frac{\partial T^*}{\partial n}(p, q; x, y) dS, \\ H_{2i}^{(k)}(x, y) &= \int_{\Gamma^k} d_i^{(k)} \frac{\partial T^*}{\partial n}(p, q; x, y) dS, \\ G_{1i}^{(k)}(x, y) &= \int_{\Gamma^k} (1 - d_i^{(k)}) T^*(p, q; x, y) dS, \\ G_{2i}^{(k)}(x, y) &= \int_{\Gamma^k} d_i^{(k)} T^*(p, q; x, y) dS. \end{aligned}$$

We are now interested in applying the methods described above to obtain heat distribution in the human eye. The following section is dedicated to numerical applications of Algorithms 1 and 2 on the problem of heat distribution in the human eye.

## 5 Numerical results and discussion

In this section, to confirm the performance of the proposed methods, synthetic tests in which the analytic expression of the solution is known are presented then real numerical experiments have been carried out using data reported in the literature.

### 5.1 Synthetic tests

The first set of tests are done using an example of the problem (5) where the analytical expression of the solution is

$$\begin{aligned} T_{exc}(x, y) &= \cos(x + y), & k(x, y) &= \exp(-x - y), \\ \omega_b \rho_b c_b &= \cos\left(\frac{\pi}{4}x\right) \sin\left(\frac{\pi}{4}y\right), & h_{bl} = h_{amb} &= \sigma \varepsilon = 1. \end{aligned}$$

For all numerical experiments  $Tol$  is set to be  $10^{-7}$ . The mesh of discretization is taken as  $h = 0.00039$ . The initial guess  $\psi_0$  and  $\mu_0$  are chosen  $\psi_0 = \mu_0 = 1$ . Figure 3 obtained by Algorithm 1, shows that the accuracy error decreases as a function of number of iterations but it took 150 iterations to reach the wanted accuracy. Figures 4 and 5 given by Algorithm 1, shows the evolution of the accurate error  $\|T_{exc} - T_1^k\|_{L^2(\partial\Omega_1)}$  on  $\Omega_1$  and  $\|T_{exc} - T_2^k\|_{L^2(\partial\Omega_2)}$  on  $\Omega_2$ , respectively as a function of the number of iteration.

In Figures 6 and 7, we can see that when using Algorithm 2, the cost and the accuracy error decrease as a function of number of iterations and reach

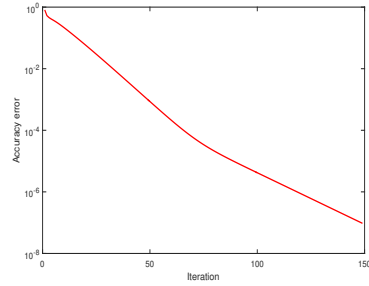


Figure 3: The accuracy error given by Algorithm 1 as a function of the number of iteration for synthetic test.

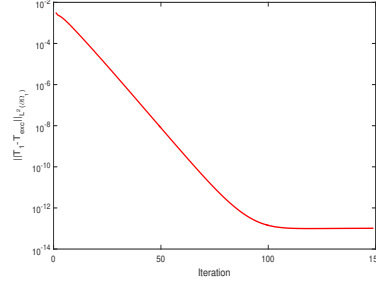


Figure 4: The accurate error  $\|T_{exc} - T_1^k\|_{L^2(\partial\Omega_1)}$  on subdomain  $\Omega_1$  given by Algorithm 1 as a function of the number of iteration for synthetic test.

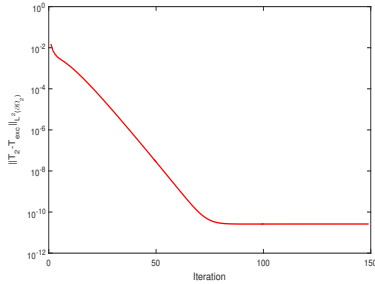


Figure 5: The accurate error  $\|T_{exc} - T_2^k\|_{L^2(\partial\Omega_2)}$  on subdomain  $\Omega_2$  given by Algorithm 1 as a function of the number of iteration for synthetic test.

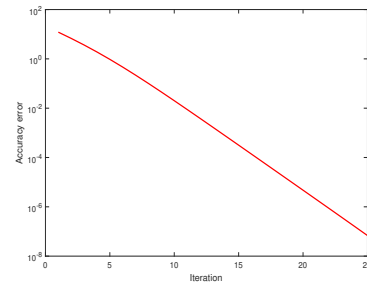


Figure 6: The accuracy error given by Algorithm 2 as a function of the number of iteration for synthetic test.

the wanted accuracy only after 25 iterations. Figure 8 given by Algorithm 2, presents the evolution of the accurate error  $\|T_{exc} - T_1^k\|_{L^2(\partial\Omega_1)}$  on  $\Omega_1$  as a function of the number of iteration, while, Figure 9 is the evolution of the accurate error  $\|T_{exc} - T_2^k\|_{L^2(\partial\Omega_2)}$  on  $\Omega_2$  as a function of the number of iteration using the same Algorithm. The discrepancy  $\|T_{exc} - T^k\|_{L^2(\partial\Omega)}$  between the exact solution and the approached one is equal to  $8.78 \times 10^{-6}$  for the DRBEM, while it is equal to  $7.81 \times 10^{-10}$  for Algorithm 1 and  $1.13 \times 10^{-9}$  for Algorithm 2. On the other side, the discrepancy  $\|Q_{exc} - Q^k\|_{\infty}$  between

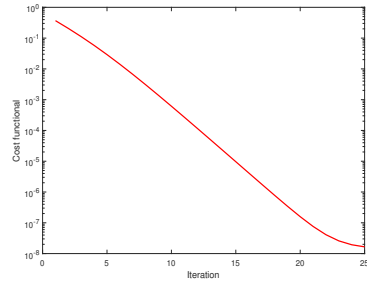


Figure 7: The cost given by Algorithm 2 as a function of the number of iteration for synthetic test.

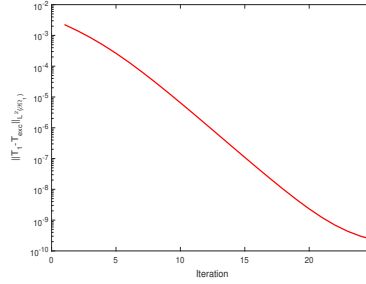


Figure 8: The accurate error  $\|T_{exc} - T_1^k\|_{L^2(\partial\Omega_1)}$  on subdomain  $\Omega_1$  given by Algorithm 2 as a function of the number of iteration for synthetic test.

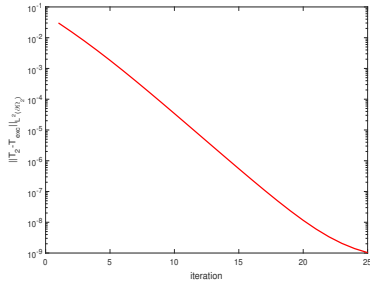


Figure 9: The accurate error  $\|T_{exc} - T_2^k\|_{L^2(\partial\Omega_2)}$  on subdomain  $\Omega_2$  given by Algorithm 2 as a function of the number of iteration for synthetic test.

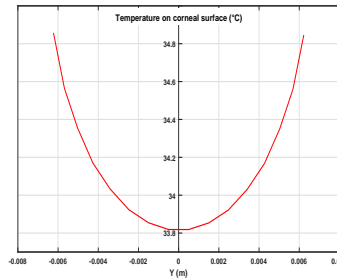


Figure 10: Temperature on the corneal surface ( $^{\circ}C$ ) obtained by DRBEM without domain decomposition for realistic experiments.

the exact normal flux and the approached one is  $4.45 \times 10^{-5}$  for the DRBEM, while it is equal to  $2.25 \times 10^{-6}$  for Algorithm 1 and  $2.53 \times 10^{-6}$  for Algorithm 2.

## 5.2 Experiments with real data

One of the main contributions of this paper is to present a 2D model of heat distribution in human eye using dual reciprocity boundary element method in conjunction with domain decomposition method. Experiments

were performed using parameters reported in Table 1.

### 5.2.1 Dual reciprocity boundary element method without domain decomposition

The heat distribution on the surface of the cornea is presented in Figure 10. The lowest temperature is  $33.8188^{\circ}C$  and is located at the center of the cornea, the highest temperature is  $36.9310^{\circ}C$  and occurs at the optic nerve where the blood is acting as a heating source. Figure 11 plots the temperature variation along pupillary axis. Figure 12 presents the heat flux distribution on the corneal surface.

### 5.2.2 Dirichlet-Neumann domain decomposition method

In this part, the human eye is decomposed into two disjoint sub-domains  $\Omega_1$  and  $\Omega_2$ . The Dirichlet-Neumann Algorithm presented in Algorithm 1, is applied to solve numerically (5). In Figure 13, the lowest temperature is  $33.7974^{\circ}C$  and it occurs at the center of the cornea. The temperature increases gradually as one approaches the sclera and the optic nerve as shown in Figure 14. Figure 15 plots the heat flux on the corneal surface.

### 5.2.3 Optimal control domain decomposition method

Similarly, in this part the human eye is divided into two disjoint sub-domains  $\Omega_1$  and  $\Omega_2$ . The optimal control domain decomposition algorithm presented in Algorithm 2, is used to solve numerically (5). Figure 16 show the temperature distribution on the surface of the cornea while figure 17 presents the heat distribution along the pupillary axis. The lowest temperature is  $33.6238^{\circ}C$ , registered at the centre and the cornea and it increases as we go from the cornea toward the optic nerve. Figure 18 shows the heat flux on the corneal surface.

All numerical values of the temperature on the center of the cornea are in good agreement with measurements obtained by various experimental techniques like bolometers [13], infra-red [5, 6, 20] and contact probe [11]. The numerical values of the corneal surface temperature obtained in this study are within the temperature range between the lowest experimental value  $33.40^{\circ}C$  and the highest  $34.80^{\circ}C$ .

The numerical values of the corneal surface temperature are very close to those reported by Ng et al. [15]  $33.65^{\circ}C$  and Ooi et al. [16]  $33.68^{\circ}C$ , this can be explained by the fact that the mathematical model for the human eye is the same as the one described but they neglected the blood perfusion term and they used different numerical methods, finite element

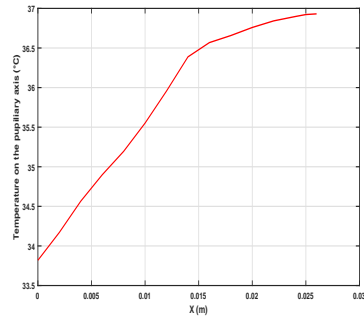


Figure 11: Temperature on the pupillary axis ( $^{\circ}C$ ) obtained by DRBEM without domain decomposition for realistic experiments.

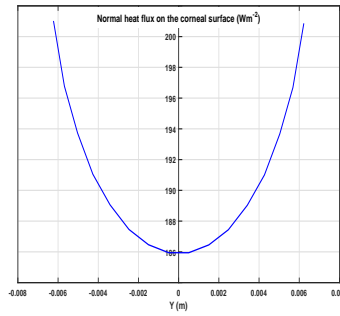


Figure 12: Normal heat flux on the corneal surface ( $Wm^{-2}$ ) calculated by DRBEM without domain decomposition for realistic experiments.

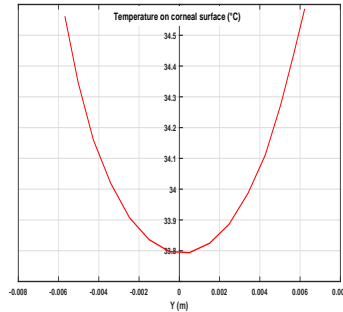


Figure 13: Temperature on the corneal surface ( $^{\circ}C$ ) obtained by Algorithm 1 for realistic experiments.

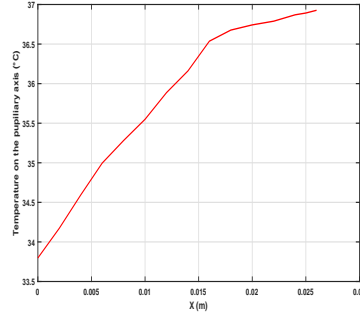


Figure 14: Temperature on the pupillary axis ( $^{\circ}C$ ) obtained by Algorithm 1 for realistic experiments.

method for [15] and boundary element method for [16]. A more considerable difference between the temperature on the center of the cornea obtained in this study and those reported by Scott [21] and Amara [1] is expected. In [21] and [1], they used a different model of the human eye.

As anticipated, the temperature on the pupillary axis increases from the lowest value at the center of the cornea where we have cooling mechanisms to the highest value at the sclera where the blood is acting as heating

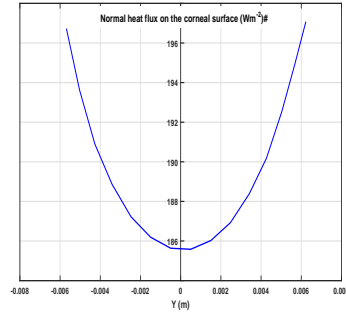


Figure 15: Normal heat flux on the corneal surface ( $Wm^{-2}$ ) calculated by Algorithm 1 for realistic experiments.

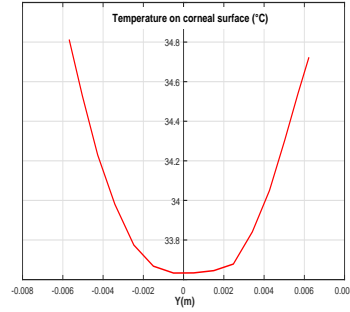


Figure 16: Temperature on the corneal surface ( $^{\circ}C$ ) obtained by Algorithm 2 for realistic experiments.

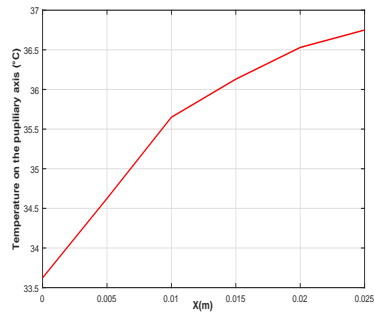


Figure 17: Temperature on the pupillary axis ( $^{\circ}C$ ) calculated by Algorithm 2.

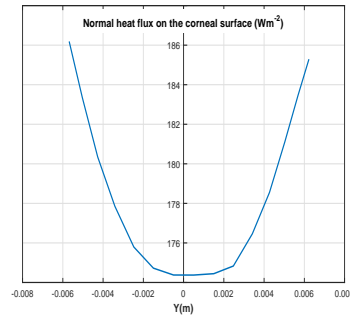


Figure 18: Normal heat flux on the corneal surface ( $Wm^{-2}$ ) obtained by Algorithm 2 for realistic experiments.

source.

## 6 Conclusion

In this paper, temperature distribution in the human eye is computed using three different methods namely, dual reciprocity boundary element method (DRBEM), Dirichlet-Neumann domain decomposition method in conjunction with DRBEM and a combination of a non-overlapping optimal control

domain decomposition method and DRBEM. All three methods used in this study were formulated and presented in details and they were validated numerically using an example where the analytical expression of the solution is known. Then numerical investigations of heat distribution in the human eye were done using realistic values for control parameters such as thermal conductivities of local tissues, blood perfusion, blood temperature and tear evaporation rate. The numerical values of heat distribution are in good agreement with values reported by previous experimental and numerical studies.

## References

- [1] E.H. Amara, *Numerical investigations on thermal effects of laser ocular media interaction*, Int. J. Heat. Mass. Tran. **38** (1995) 2479–2488.
- [2] I. Bogalev, *A block monotone domain decomposition algorithm for nonlinear singularly perturbed parabolic problem*, Int. J. Numer. Anal. Model. **3**(2) (2006) 211–231.
- [3] M.W. Charles and N. Brown, *Dimensions of the human eye relevant to radiation protection*, Phys. Med. Biol. **20**(2) (1975) 202–218.
- [4] U. Cicekli, *Computational model for heat transfer in the human eye using the finite element method*, M.Sc. Thesis, Department of Civil and Environmental Engineering, Louisiana State University, 2003.
- [5] N. Efron, G. Young and N.A. Brennan, *Ocular surface temperature*, Curr. Eye Res. **8**(9) (1989) 901–906.
- [6] A.R. Fielder, A.F. Winder, G.A.K. Sheridaidah and E.D. Cooke, *Problems with corneal arcus*, Trans. Ophthalmol. Soc. U. K. **101**(1) (1981) 22–26.
- [7] S.T. Fontana and R.F. Brubaker, *Volume and DOF the anterior chamber of the normal aging human eye*, Arch. Ophthalmol. **98**(10) (1980) 1803–1808.
- [8] J. Goodman, *Newton's method for constrained optimization*, Math. Program. **33**(2) (1985) 162–171.
- [9] K. Gokul, G. Dil Bahadur and R. Pushpa, *FEM approach for transient heat transfer in human eye*, Appl. Math. **4**(10) (2013) 30–36.

- [10] A. Holmberg, *The temperature of the eye during application of hot packs and after milk injections*, *Acta Ophthalmol. (Copenhagen)* **30** (1952) 347–360.
- [11] I. Horven and C.T. Larsen, *Contact probe for corneal temperature measurements*, *Acta Ophthalmol.* **53**(6) (1975) 856–862.
- [12] J.J.W. Lagendijk, *A mathematical model to calculate temperature distributions in human and rabbit eyes during hyperthermic treatment*, *Phys. Med.* **27** (1982) 1301–1311.
- [13] R. Mapstone, *Measurement of corneal temperature*, *Exp. Eye Res.* **7** (1968) 237–243.
- [14] A. Narasimhan, K. K. Jha and L. Gopal, *Transient simulations of heat transfer in human eye undergoing laser surgery*, *Int. J. Heat Mass Tran.* **53**(1-3) (2010) 482–490.
- [15] E.Y.K. Ng and E.H. Ooi, *FEM simulation of the eye structure with bio-heat analysis*, *Comput. Methods. Programs. Biomed.* **82** (2006) 268–276.
- [16] E.H. Ooi, W.T. Ang and E.Y.K. Ng, *Bioheat transfer in the human eye: A boundary element approach*, *Eng. Anal. Bound. Elem.* **3** (2007) 494–500.
- [17] E.H. Ooi and E.Y.K. Ng, *Simulation of aqueous humor hydrodynamics in human eye heat transfer*, *Comput. Biol. Med.*, **38**(2) (2008) 252–262.
- [18] H.H. Pennes, *Analysis of tissue and arterial blood temperatures in the resting human forearm. 1948.*, *J. Appl. Physiol.* **85** (1998) 5–34.
- [19] C. Purslow, J.S. Wolffsohn and J. Santodomingo-Rubido, *The effect of contact lens wear on dynamic ocular surface temperature*, *Cont. Lens. Anterior Eye.* **25**(1) (2005) 29–36.
- [20] P. Rysa and J. Sarvaranta, *Thermography of the eye during cold stress*, *Acta Ophthalmol.* **123** (1973) 234–239.
- [21] J.A. Scott, *A finite element model of heat transport in the human eye*, *Phys. Med. Biol.* **33** (1988) 227–241.
- [22] H. Wang and Q.H. Qin, *FE approach with Greens function as internal trial function for simulating bioheat transfer in the human eye*, *Arch. Mech.* **62**(6) (2010) 493–510.